Chemical Science

ROYAL SOCIETY OF CHEMISTRY

EDGE ARTICLE

View Article Online
View Journal

Cite this: DOI: 10.1039/d6sc00914j

All publication charges for this article have been paid for by the Royal Society of Chemistry

Real-time NIR-II fluorescence imaging-guided precision thrombolysis with a molecularly planarized phototheranostic agent

Guosheng Zhang,[ac] Leilei Si,[ab] Fuhai Zhou,[ab] Xiaofang Song[ab] and Hongming Wang *[ab]

The precise diagnosis and treatment of intravascular thrombosis pose a major clinical challenge, as existing technologies struggle to simultaneously achieve high-resolution imaging and highly efficient yet safe therapy. To address this, we propose a molecular planarization engineering strategy. Based on the benzo[*cd*]indol-2(1*H*)-one scaffold, phenyl/biphenyl groups were introduced at the 6-position to construct a D–A–D type squaraine dye, SQ-BiPh. This strategy significantly extends the π-conjugation system and enhances molecular rigidity. Notably, the molecule forms a well-defined J-aggregate structure after nanoencapsulation, which substantially red-shifts the absorption peak to 1087 nm, extends the emission wavelength beyond 1130 nm, and simultaneously endows the material with excellent photothermal conversion performance. The corresponding nanoparticles (SQ-BiPh NPs) enable simultaneous high-contrast NIR-II fluorescence imaging and precise 1064 nm laser-triggered photothermal thrombolysis in a mouse model of lower-extremity venous thrombosis, allowing real-time monitoring of thrombus dissolution and vascular recanalization. This work not only establishes a new, generalizable molecular design paradigm for developing high-performance NIR-II phototheranostic agents but also successfully constructs an efficient, safe, and integrated platform for precise thrombus theranostics.

Received 2nd February 2026
Accepted 16th April 2026

DOI: 10.1039/d6sc00914j

rsc.li/chemical-science

Introduction

Thrombosis, the common pathological basis of fatal cardiovascular events such as acute myocardial infarction, ischemic stroke, and pulmonary embolism, contributes to nearly 18 million deaths worldwide annually, imposing a substantial global disease burden.[1–4] Effective and safe thrombolysis critically depends on achieving real-time, image-guided precision therapy, which necessitates the seamless integration of three core components: precise visualization, targeted delivery, and localized controllable intervention.[5,6] However, significant limitations in current clinical paradigms at both the diagnostic and therapeutic fronts fundamentally hinder this goal.[7,8]

Conventional thrombolytic therapy, epitomized by tissue plasminogen activator (t-PA), relies on a systemic administration model plagued by critical shortcomings.[9,10] Its lack of active targeting results in less than 5% of the drug dose reaching the thrombotic site, necessitating high systemic concentrations that elevate the risk of life-threatening hemorrhagic complications, particularly intracranial hemorrhage (incidence: 6–8%).[11–13] This narrow risk-benefit ratio severely restricts its therapeutic window.[14,15] In parallel, the "golden time window" for intervention is often compromised by diagnostic ambiguity. Current imaging modalities like ultrasound and magnetic resonance imaging frequently lack the sensitivity, resolution, or speed required for the reliable detection of small, non-occlusive, or deep-seated thrombi, failing to provide the real-time, high-fidelity anatomical and functional data needed to guide precise therapeutic decisions.[16,17] This synergy of imprecise treatment and ambiguous diagnosis underpins the high rates of recurrence and disability in thrombotic diseases, highlighting an urgent need for a novel integrated strategy.[18]

The convergence of second near-infrared (NIR-II) fluorescence imaging and photothermal therapy (PTT) presents a compelling technological pathway towards real-time, image-guided precision thrombolysis.[19–21] NIR-II imaging offers superior tissue penetration, high spatial resolution, and minimal background interference, making it ideal for real-time, precise visualization of vascular structures and thrombi.[22–24] Crucially, the photothermal effect allows NIR-II light energy to be locally converted into heat, enabling controlled and localized intervention (ablation/thrombolysis) under direct imaging guidance, thus providing a unified theranostic platform.[25–27] However, the realization of this integrated vision is obstructed by a fundamental materials science bottleneck: the intrinsic trade-off in the photophysical properties of NIR-II agents.[28,29] Most reported probes cannot

[a]*Jiangxi Provincial Key Laboratory of Functional Crystalline Materials Chemistry, Nanchang 330031, China. E-mail: hongmingwang@ncu.edu.cn*

[b]*College of Chemistry and Chemical Engineering, Nanchang University, Nanchang 330031, China*

[c]*Information Engineering College, Nanchang University, Nanchang 330031, China*

synergistically achieve the triad of high molar extinction coefficient (ε), high fluorescence quantum yield (Φ_F), and high photothermal conversion efficiency (PCE).[30]

This performance "see-saw" arises because molecular designs favoring high PCE (*e.g.*, twisted conformations promoting non-radiative decay) often compromise ε and Φ_F, yielding weak imaging signals.[31,32] Conversely, structures optimized for bright fluorescence (planar, rigid) typically exhibit limited non-radiative channels, hindering efficient photothermal conversion. Consequently, existing agents are inadequate for simultaneously meeting the dual demands of high-contrast real-time imaging and high-efficacy therapy, stalling the translation of NIR-II theranostics for thrombosis.[33–35]

To resolve this contradiction, a paradigm shift in molecular design is required-one that enables synergistic regulation of excited-state energy allocation.[36] Theoretical insights suggest that enhancing molecular rigidity and planarity could be key, as it extends π-conjugation (improving ε, red-shifting absorption), suppresses unproductive intramolecular motions, and potentially optimizes energy pathways for both radiative decay (fluorescence) and efficient non-radiative relaxation (photothermal).[37–40] Inspired by this, we propose a "molecular planarization engineering" strategy. Using benzo[*cd*]indol-2(1*H*)-on, an inherently rigid and electron-deficient core, we constructed a series of squaraine dyes *via* systematic arylation at the 6-position, enhancing donor–acceptor–donor (D–A–D) characteristics to maximize the planarity and rigidity of the conjugated system.[41]

This paper reports the high-performance theranostic probe SQ-BiPh and its nanoparticle formulation derived from this strategy. SQ-BiPh NPs exhibits a pronounced absorption at 1087 nm ($\varepsilon \approx 1.08 \times 10^5$ M^{-1} cm^{-1}), an emission beyond 1130 nm, a Φ_F of 0.274%, and excellent PCE, achieving a synergistic breakthrough. Leveraging these properties, SQ-BiPh nanoparticles enabled precise localization and real-time visualization of thrombi *via* NIR-II fluorescence imaging in a murine model of lower-extremity venous thrombosis. Subsequently, efficient photothermal thrombolysis was achieved under 1064 nm laser irradiation, with the entire vascular recanalization process dynamically monitored in real-time, all without significant systemic toxicity or increased bleeding risk. This work validates the molecular planarization strategy for developing advanced NIR-II theranostics and provides an integrated, efficient, and safe solution-from molecular design to *in vivo* demonstration-for real-time, image-guided precision thrombolysis, directly addressing enduring challenges in the management of thrombotic diseases.

Results and discussion

Molecular design, synthesis, and characterization

Benzo[*cd*]indol-2(1*H*)-one, a lactam scaffold characterized by its rotor effects and electron-deficient nature, exhibits strong electron-donating capabilities and multiple modifiable sites, providing great design flexibility for constructing high-

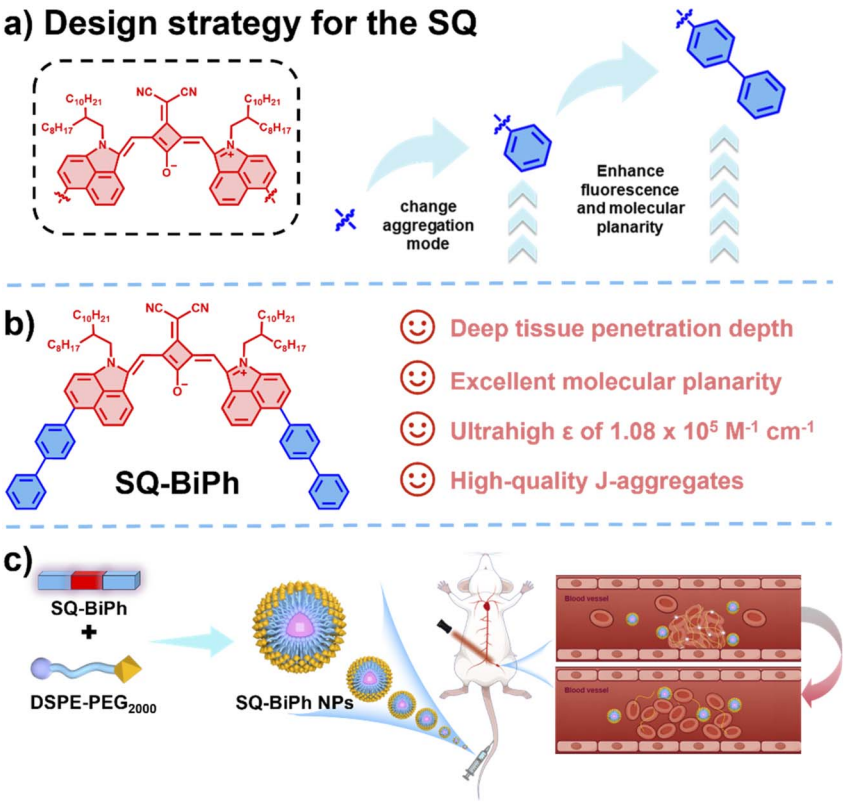

Scheme 1 (a) Strategy for molecular design and structure of NIR-II D–A–D fluorescent probes. (b) chemical structure and design concept of the representative molecule SQ-BiPh developed in this work. (c) Schematic illustration of fluorescence imaging (FLI) and photothermal thrombolysis-guided photothermal therapy (PTT).

performance and highly specific NIR-II fluorescent probes. To leverage these features, we developed a novel molecular design strategy: systematically introducing phenyl and biphenyl groups at the 6-position of benzo[*cd*]indol-2(1*H*)-one to replace the original hydrogen atom, thereby constructing a series of derivatives with enhanced electron-donating capabilities. These strong donor units were then coupled with a strong electron-accepting squaraine receptor modified with malononitrile *via* efficient condensation reactions, resulting in the formation of D–A–D type derivatives designated as SQ-H, SQ-Ph, and SQ-BiPh (Scheme 1). The extended conjugation in the SQs molecules enhanced molecular rigidity and planarity, expanding the range of electron delocalization. This structural optimization not only resulted in a bathochromic shift in the absorption/emission spectra but also significantly increased the molar extinction coefficient. The synthesis was accomplished with Suzuki coupling as a key step, affording the target compounds in high yields (detailed synthetic routes are provided in Fig. S1, SI). All intermediates and final products were unambiguously characterized by $^{1}H/^{13}C$ NMR spectroscopy (Fig. S2–S5, SI) and high-resolution mass spectrometry.

To gain deeper insights into the structure–photophysical property relationships, we shortened the branched alkyl chain length and successfully obtained single crystals of SQ-H-S, SQ-Ph-S, and SQ-BiPh-S *via* diffusion of a poor solvent (dichloromethane/*n*-hexane). The crystallographic data and refinement parameters are summarized in Table S1, enabling a detailed analysis of their corresponding packing patterns and intermolecular interactions. Through single-crystal structure analysis, we observed progressively decreasing dihedral angles between the central malononitrile-modified squaraine unit and the adjacent benzo[*cd*]indol-2(1*H*)-one moiety, as illustrated in Fig. 1b. This trend reveals that extended conjugation leads to increasingly planar molecular structures. To further elucidate the structural and electronic implications of different donor units in the SQs series, we performed calculations using Density Functional Theory (DFT, B3LYP/6-311G*).[42] As shown in Fig. 1c, the energy gap between the lowest unoccupied molecular orbital (LUMO) and the highest occupied molecular orbital (HOMO) decreases with increasing conjugation, which can be attributed to the extension of the conjugated system. The introduction of conjugated phenyl rings drives the rotation of cross-molecules around the π–π interaction axis, while the phenyl and biphenyl groups act as hydrogen bond donors, forming interlocked hydrogen bonds with electron-deficient oxygen atoms, thereby further stabilizing molecular rotation. Under the combined and synergistic effects of these interactions, SQ-Ph-S and SQ-BiPh-S form slipped parallel dipole–dipole stacked J-aggregates. Further photophysical characterization revealed that the absorption spectra of both SQ-Ph-S and SQ-BiPh-S exhibit typical J-aggregate features, and the absorption spectra of their respective long-chain counterparts also display similar J-aggregate

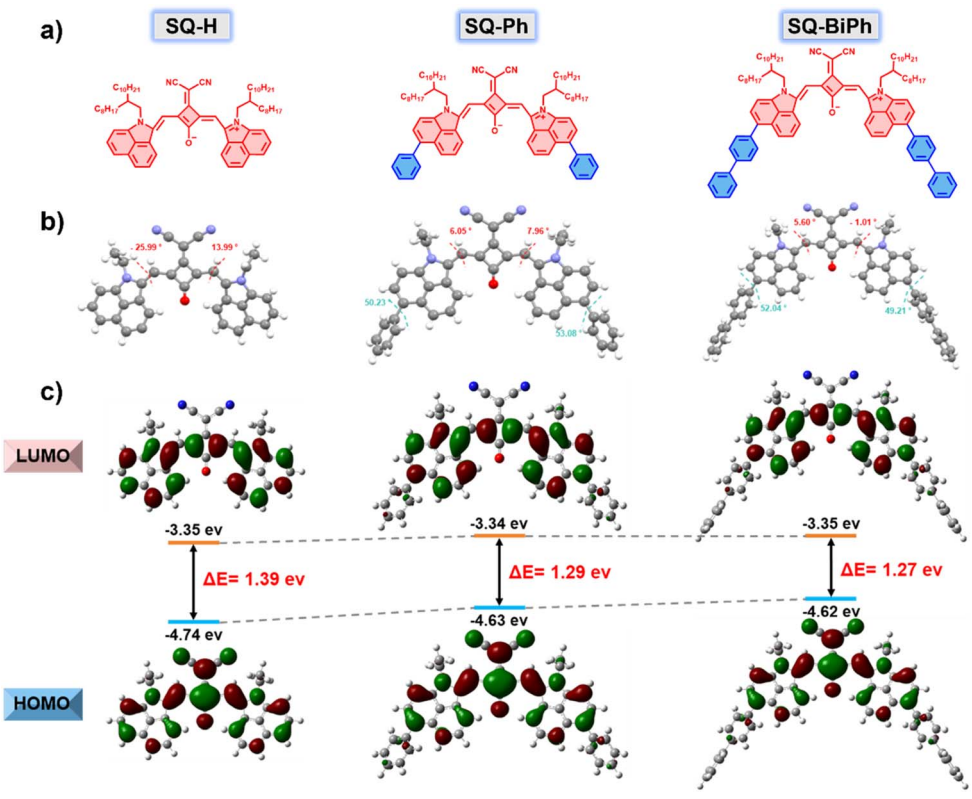

Fig. 1 (a) Chemical structures, (b) molecular structure from single-crystal data (c) the highest occupied molecular orbitals (HOMO) and the lowest unoccupied molecular orbitals (LUMO) distributions of SQ-H, SQ-Ph and SQ-BiPh. In order to facilitate the cultivation of single crystals, all long alkyl chains have been replaced with ethyl groups.

behavior, and such J-aggregation can form over a broad temperature range (Fig. S6 and S7, SI). Additionally, the steric hindrance provided by the phenyl and biphenyl groups restricts the rotation of the Np segment, resulting in enhanced molecular planarity in SQ-Ph-S and SQ-BiPh-S. This improvement strengthens their light-harvesting capacity, implying an elevated upper limit for the total convertible photons.

Crystal packing and fluorescence tuning and Hirshfeld surface study

To further elucidate the mechanism underlying changes in π–π stacking upon phenyl and biphenyl incorporation, quantitative Hirshfeld surface analysis was performed in conjunction with crystal structure examination.[43] As shown in Fig. 2a–c, SQ-BiPh-S and SQ-Ph-S formed aggregates distinctly different from those of SQ-H, indicating a clear aggregation-state transition, which aligns with conclusions from our previous work.[44] On one hand, the proportion of C···C contacts decreased to 9.6% from SQ-H-S to SQ-BiPh-S, suggesting that the introduction of aromatic rings effectively suppressed intermolecular π–π stacking and modulated molecular packing behavior.[45] On the other hand, the higher proportion of C···H interactions (31.4%) in SQ-BiPh-S mainly occurring between hydrogen atoms in alkyl chains and the conjugated plane of donor aromatic rings-contributed to structural rigidification and enhanced molecular planarity through mediating intermolecular interactions.[46]

To probe the driving forces behind these interactions, we performed electrostatic potential (ESP) calculations (Fig. 2d–f). Results indicated that nitrogen atoms in the malononitrile group and oxygen atoms in the squaraine unit exhibit substantially negative ESP values, while hydrogen atoms in ethyl groups show positive ESP. These complementary electrostatic characteristics facilitate ordered molecular packing, leading to more rigid aggregate structures and effective suppression of molecular motion.

Attributed to the above factors, significant bathochromic shifts in absorption/emission were observed in the NIR-II region. For instance, compared to SQ-H in THF, the more planar SQ-BiPh exhibited an absorption redshift from 940 nm to 990 nm (Fig. 2g and Table S3, SI). We further evaluated their fluorescence performance under common laser excitations at 980 nm and 1064 nm (Fig. 2h and i). As envisioned in our molecular design, SQ-BiPh demonstrated superior fluorescence emission and enhanced luminescence efficiency. These optimized photophysical properties and well-defined solid-state packing modes render these compounds, particularly SQ-

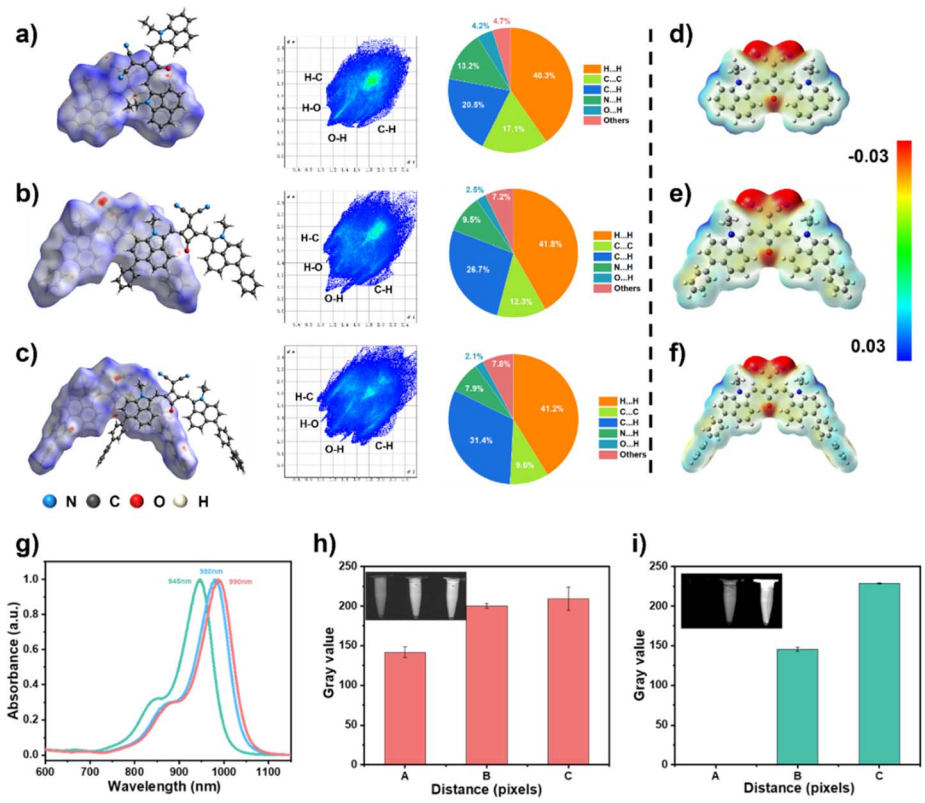

Fig. 2 (a–c) Hirshfeld surface analysis and corresponding full fingerprint plots for (a) SQ-H, (b) SQ-Ph, and (c) SQ-BiPh. (d–f) Electrostatic potential (ESP) maps of (d) SQ-H, (e) SQ-Ph, and (f) SQ-BiPh. (g) Normalized absorption spectra of SQ-H, SQ-Ph, and SQ-BiPh in THF. (h) Fluorescence emission images and quantitative analysis of SQ-H, SQ-Ph, and SQ-BiPh (from left to right) under 980 nm laser excitation. Imaging conditions: 980 nm excitation, 980 nm long-pass filter, laser power density of 0.3 W cm^{-2}, exposure time of 100 ms. (i) Fluorescence emission images and quantitative analysis of SQ-H, SQ-Ph, and SQ-BiPh (from left to right) under 1064 nm laser excitation. Imaging conditions: 1064 nm excitation, 1064 nm long-pass filter, laser power density of 0.3 W cm^{-2}, exposure time of 100 ms.

BiPh, highly promising for subsequent applications in NIR-II fluorescence imaging and phototheranostics.

The UV-vis-NIR absorption spectra of SQ-BiPh in various organic solvents exhibited narrow absorption profiles extending beyond 800 nm (Fig. S8, SI). J-aggregate formation was investigated through solvent-mediated aggregation in THF/H_2O mixtures, with the temperature controlled at 0–10 °C to enable better-controlled aggregation and obtain clearer J-aggregate spectral features. Upon increasing the aqueous fraction to 50%, SQ-BiPh demonstrated remarkable spectral evolution: the attenuation of the monomeric peak at 990 nm coincided with the emergence of a J-aggregate band at 1087 nm, with corresponding fluorescence intensity changes consistently observed in parallel measurements (Fig. S9 and S10, SI).

Preparation and characterization of nanoparticles

To obtain water-dispersible probes, SQ-BiPh was encapsulated into nanoparticles (NPs) using DSPE-mPEG2000. As shown in Fig. 3a–c, the resulting SQ-BiPh NPs exhibited maximum absorption at 1087 nm and peak emission at 1130 nm. Dynamic light scattering (DLS) measurements indicated an average particle size of approximately 115 nm (Fig. 3b). Stability evaluations demonstrated that SQ-BiPh NPs exhibited excellent colloidal and photophysical stability under physiologically relevant conditions, including PBS (pH 7.4), saline, and serum-containing medium, as evidenced by negligible changes in absorption spectra, particle size, and zeta potential, along with sustained particle size stability upon prolonged storage. Furthermore, no significant variations in absorption spectra or particle size were observed under varying pH and ionic strength conditions (Fig. S11–S13, SI). It is worth emphasizing that the encapsulation efficiency of this system reached as high as 96.5% (Fig. S14, SI), indicating highly efficient loading of SQ-BiPh into the nanoparticles.

Under 1064 nm laser excitation, the NIR-II fluorescence intensity of SQ-BiPh NPs increased linearly with concentration (Fig. 3d), demonstrating their potential for quantitative imaging. Using IR1061 as a reference, the fluorescence quantum yield of SQ-BiPh NPs in the NIR-II region was determined to be 0.274% (Fig. S15, SI).[47] Penetration depth experiments revealed that the probe maintained satisfactory imaging signal-to-noise ratio even at a tissue-simulating depth of 6 mm (Fig. S16, SI), highlighting its capability for deep-tissue imaging.

In addition to fluorescence performance, SQ-BiPh NPs also exhibited remarkable photothermal conversion capability. As shown in Fig. 3e–g, the photothermal heating effect displayed significant concentration dependence, suggesting that heat output can be precisely controlled. The NPs retained excellent photothermal stability over six heating–cooling cycles (Fig. 3g). The photothermal conversion efficiency is shown in Fig. 3h. Notably, SQ-BiPh NPs exhibit favorable photothermal

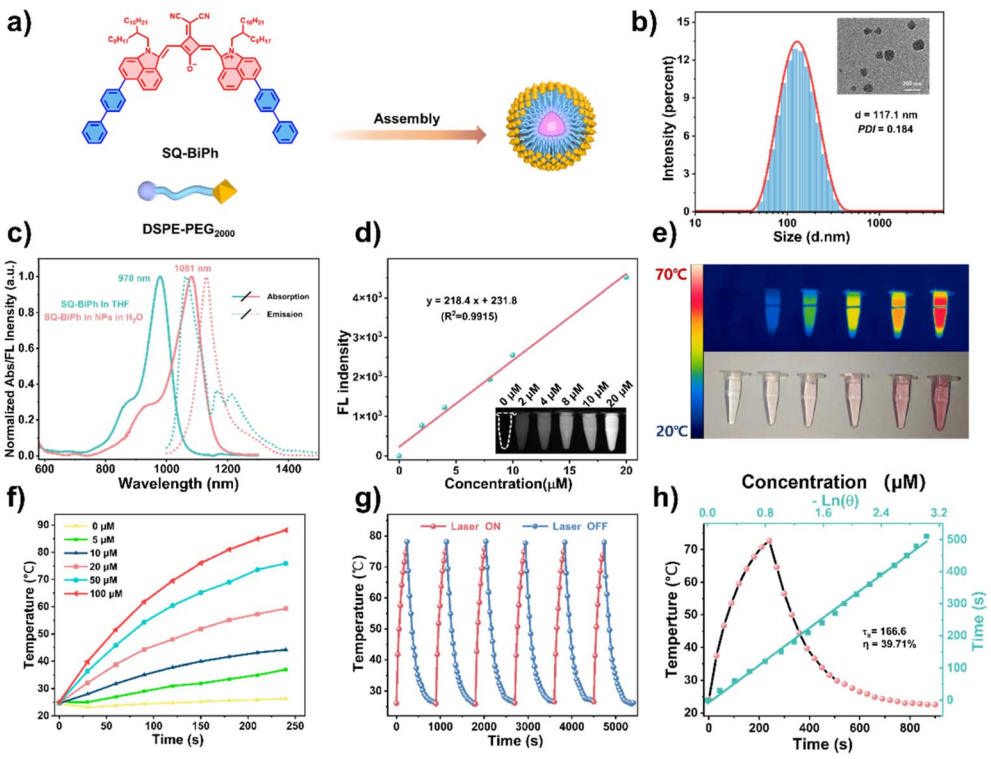

Fig. 3 (a) Schematic illustration of the synthesis of SQ-BiPh NPs. (b) Size distribution histogram image of the as-prepared SQ-BiPh NPs. (c) Absorption spectrum of the SQ-BiPh molecule in THF and the normalized absorption and emission spectra of the corresponding NPs in water. (d) Concentration-dependent fluorescence intensity of SQ-BiPh NPs under 1064 nm laser irradiation. (e and f) Infrared thermal images and corresponding photothermal heating curves of SQ-BiPh NPs aqueous solutions at different concentrations under 1064 nm laser irradiation. (g) Photothermal stability of SQ-BiPh NPs over six on/off cycles (1064 nm, 1.0 W cm^{-2}, 60 μM, 150 μL). (h) Heating curve of SQ-BiPh NPs during irradiation and the linear time data *versus* $-\ln(\theta)$ from the cooling period.

conversion efficiency; although the other two SQ derivatives show higher photothermal conversion efficiency (Fig. S17 in the SI), considering the fluorescence performance described above, the overall performance of SQ-BiPh NPs still demonstrates advantages, which is comparable to recently reported photothermal agents for thrombus therapy, further supporting their potential for integrated theranostic applications (Table S2 in the SI).

In Vivo NIR-II FL imaging

Prior to *in vivo* vascular imaging, the biocompatibility of SQ-BiPh NPs was confirmed by a cytotoxicity assay, which demonstrated low cytotoxicity (Fig. S18, SI). Leveraging the excellent fluorescence properties of SQ-BiPh NPs, we further investigated their performance in NIR-II vascular imaging in BALB/c nude mice. All animal procedures were approved by the Animal Ethics Committee of Nanchang University. As shown in Fig. 4a, after intravenous injection of SQ-BiPh NPs, the systemic vasculature immediately exhibited bright NIR-II fluorescence. By applying various long-pass (LP) filters ranging from 1150 nm to 1450 nm, we successfully achieved whole-body bioimaging, demonstrating remarkable NIR-IIb fluorescence imaging capability. Furthermore, we quantitatively analyzed the signal-to-background ratio (SBR) and full width at half maximum (FWHM) of images obtained with different LP filters, as summarized in Fig. 4b. Among these NIR-II images, the 1350 nm LP filter yielded the highest SBR, while blood vessels imaged with this filter showed the smallest FWHM, indicating superior resolution at this wavelength. These results align with previous experimental observations: strong water absorption at 1450 nm significantly suppresses background signals generated by scattered light, leading to a higher SBR with the 1350 nm LP filter compared to the 1450 nm LP filter.

Using this optimized NIR-II imaging setup, we performed high-resolution angiography of localized vasculature in the mouse brain, dorsal region, abdomen, and hindlimbs under 1350 nm LP filtration. All these vascular structures were clearly

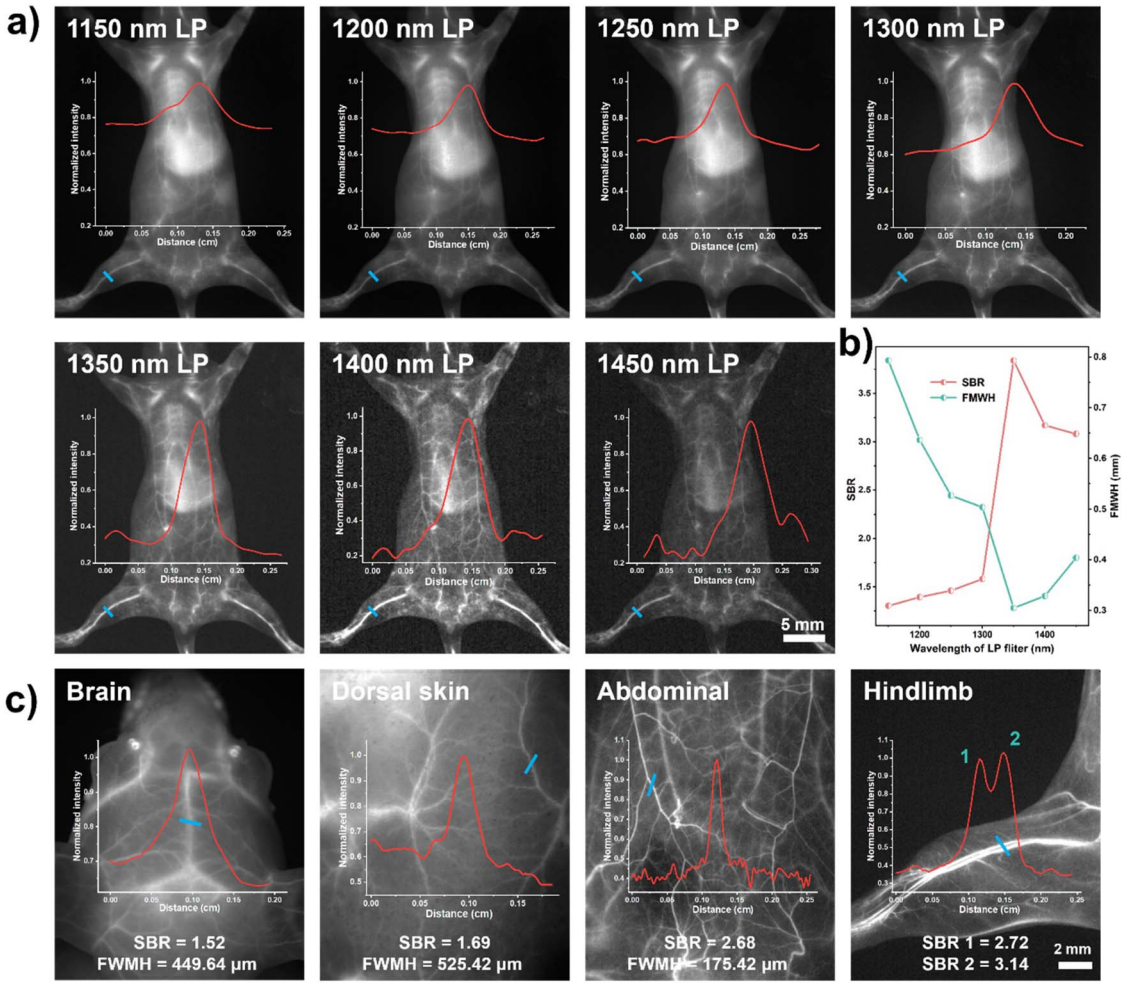

Fig. 4 (a) *In vivo* whole-body NIR-II imaging of mice using SQ-BiPh NPs under different long-pass (LP) filters. Imaging conditions: 1064 nm excitation, laser power density of 0.3 W cm^{-2}, exposure time of 100 ms. (b) Corresponding signal-to-background ratio (SBR) and full width at half maximum (FWHM) analysis of the tissue region marked by the blue dashed line in (a). (c) High-resolution NIR-II imaging of the brain, back, abdomen, and hindlimb vasculature labeled with SQ-BiPh NPs, captured under 1064 nm laser excitation with a 1350 nm LP filter. Imaging conditions were the same as in (a).

resolved, and the magnified images obtained with the 1350 nm LP filter consistently displayed the best SBR (Fig. 4c), highlighting the superior performance of SQ-BiPh NPs for high-resolution NIR-II angiography at this wavelength. In addition to intravenous injection, we also evaluated two alternative administration routes: intraperitoneal injection and oral gavage (Fig. S19, SI). In mice subjected to intraperitoneal injection, we clearly observed fluid distribution within the peritoneal cavity. Remarkably, intestinal peristalsis was visually tracked following oral administration. These findings underscore the promising potential of SQ-BiPh NPs for diverse biomedical applications.

In Vitro thrombolytic capability

Encouraged by the promising photothermal properties and excellent imaging performance of SQ-BiPh NPs, we proceeded to investigate their potential for thrombus dissolution. First, we evaluated the *in vitro* biosafety of SQ-BiPh NPs by co-culturing them with HUVEC cells for 24 hours. Methylthiazolyldiphenyl-tetrazolium bromide (MTT) assays indicated that over 90% of cells remained viable after treatment with 0–80 μM NPs, demonstrating minimal cytotoxicity (Fig. S18, SI). We further assessed the hemocompatibility of SQ-BiPh NPs *via* hemolysis tests. At concentrations ranging from 0 to 200 μM, the hemolysis rates of all blood samples remained below 3% (Fig. 5a), confirming excellent blood compatibility.

To evaluate thrombolytic efficacy, artificial blood clots were prepared and subjected to different treatments: (i) PBS, (ii) L, (iii) SQ-BiPh NPs, and (iv) SQ-BiPh NPs + L. Groups labeled "L" were irradiated with a 1064 nm laser (1.0 W cm^{-2}) for 20 minutes. Thrombolytic efficiency was assessed by measuring clot dissolution rates and the UV absorption of fibrin and hemoglobin released from the clots. After treatment with "SQ-BiPh NPs + L," the clots showed a significant reduction in size, and the supernatant turned dark red, indicating substantial release of fibrin and hemoglobin (Fig. 5b–d). Furthermore, we performed hematoxylin and eosin (H&E) staining on the residual clots to visualize thrombolytic effects (Fig. 5f). While clots treated with L or SQ-BiPh NPs + L exhibited surface roughness and structural damage, the SQ-BiPh NPs + L group displayed the most pronounced clot degradation. Collectively, these results demonstrate that SQ-BiPh NPs significantly enhance thrombus dissolution through photothermal therapy.

SQ-BiPh NPs for *in vivo* antithrombotic therapy

Based on prior *in vitro* experiments confirming the excellent photothermal thrombolytic efficacy and biocompatibility of SQ-BiPh NPs, we systematically evaluated their theranostic performance in a lower-extremity venous thrombosis model in female BALB/c mice. This involved real-time monitoring of thrombus progression *via* NIR-II fluorescence imaging and precise

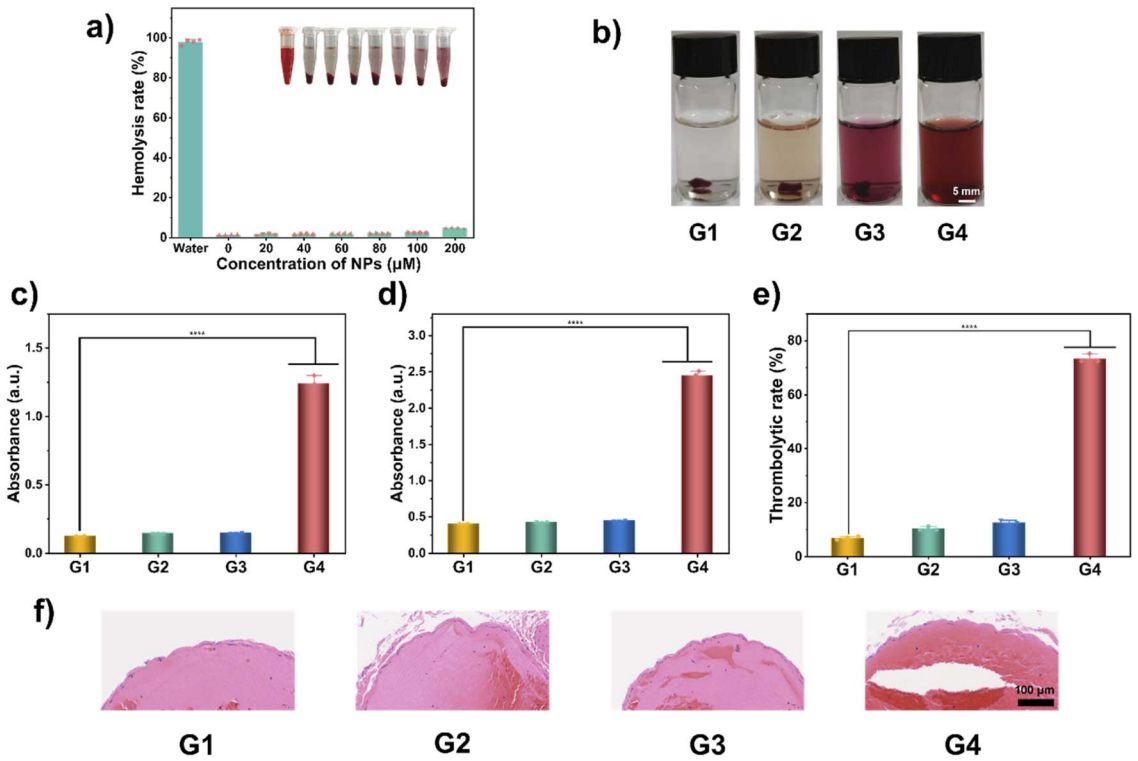

Fig. 5 *In vitro* thrombolytic properties of SQ-BiPh NPs. (a) Hemocompatibility evaluation of SQ-BiPh NPs *via* red blood cell hemolysis assay. (b) Photographs of artificial thrombi after different treatments. Scale bar: 5 mm. Changes in (c) fibrin and (d) hemoglobin levels in the supernatant of artificial thrombi following various treatments. (e) Thrombolytic efficacy of different treatments on artificial thrombi. (f) H&E stained images of artificial thrombi after various treatments. Scale bar: 100 μm. Data are presented as mean ± SD ($n = 3$). Statistical significance was determined by one-way ANOVA analysis. G1: PBS group; G2: PBS + laser group; G3: SQ-BiPh NPs (200 μM) group; G4: SQ-BiPh NPs (200 μM) + laser group. Imaging conditions: 1064 nm excitation, laser power density of 0.3 W cm^{-2}.

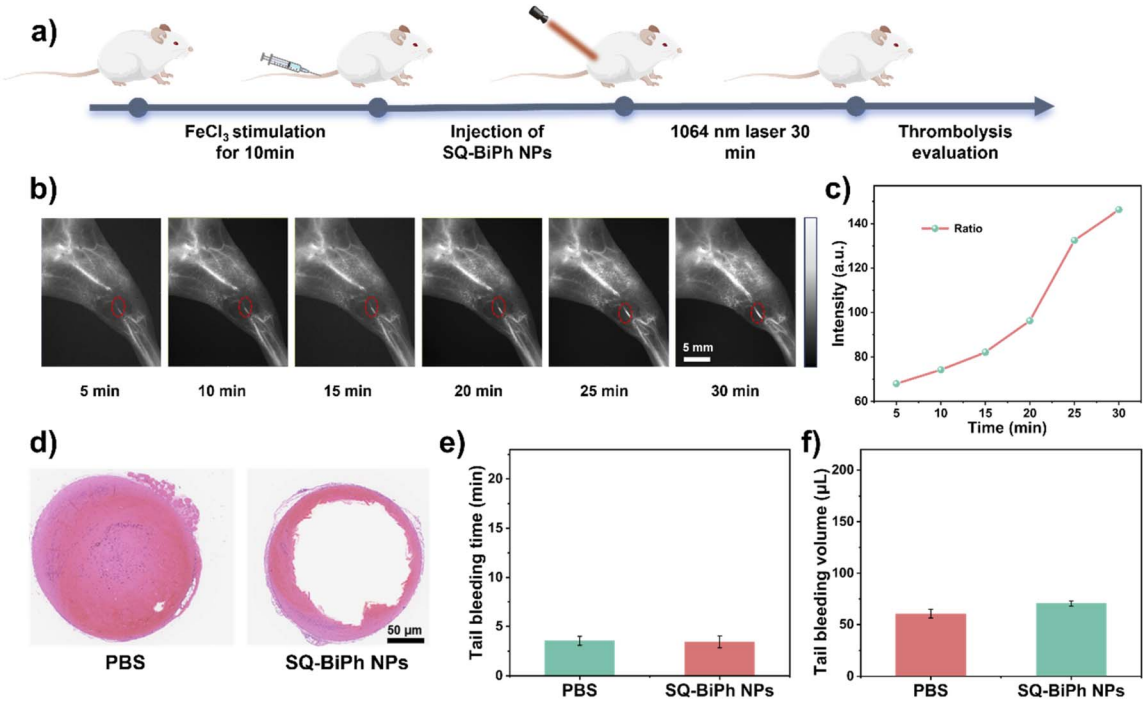

Fig. 6 Monitoring vascular recanalization and evaluating thrombolytic efficacy *via* NIR-II imaging in bilateral lower limbs (right femoral artery thrombus model). (a) Schematic diagram of the *in vivo* experiments in mice. (b) NIR-II images after intravenous injection of SQ-BiPh NPs (100 μL, 200 μM) followed by 1064 nm laser irradiation (0.5 W cm^{-2}, 30 min). (c) Fluorescence intensity changes within the red dashed areas. (d) H&E staining of femoral artery thrombus sites after different treatments (PBS + L and SQ-BiPh NPs + L). (Light irradiation: 1064 nm laser, 0.5 W cm^{-2}, 30 min). Scale bar: 50 μm. (e) Tail bleeding time. (f) Tail bleeding volume.

thrombolytic treatment through photothermal effects (Fig. 6a). To ensure experimental consistency, both hindlimbs underwent identical surgical procedures: the right hindlimb served as the experimental side for modeling and treatment, while the left hindlimb received the same degree of epidermal excision and femoral artery exposure as a control. Due to the limited field of view of the NIR-II imaging system, we were unable to simultaneously capture images of both hindlimbs. Therefore, the fluorescence images of the left hindlimb during the treatment process are presented separately (SI Fig. S20). As shown in Fig. S20, the vascular signal in the left hindlimb remained clear and intact throughout the experiment, with no signal interruption, indicating that the surgical procedure itself did not cause vascular injury or occlusion.

To clarify the photothermal therapeutic effect mediated by SQ-BiPh NPs, we monitored vascular recanalization during-thrombus dissolution using NIR-II imaging. Before intravenous injection of SQ-BiPh NPs, the right hindlimb was irradiated with a 1064 nm laser (0.5 W cm^{-2}) for 5 minutes. NIR-II imaging confirmed that the femoral artery remained occluded, indicating that laser irradiation alone was insufficient to dissolve the thrombus. However, in subsequent irradiation after injection of SQ-BiPh NPs, a significant recovery of the previously absent NIR-II signal due to thrombosis was observed with increasing cumulative irradiation time, suggesting gradual revascularization of the lower extremity vein (Fig. 6b and c). During the laser irradiation process, we monitored the real-time temperature changes at the thrombus site and modulated the laser output to maintain the local temperature at approximately 50 °C (maximum 49.4 °C), thereby avoiding thermal damage to surrounding tissues caused by sustained high temperatures (SI Fig. S21 and S22). Meanwhile, to further evaluate the thermal safety of the photothermal thrombolysis process on tissues surrounding the irradiation area, we collected peri-irradiation tissues for H&E staining analysis. The results showed no obvious thermal damage, inflammatory cell infiltration, or tissue necrosis in the tissues surrounding the laser irradiation area (SI Fig. S23), indicating that local heating around 50 °C achieves effective thrombolysis while maintaining good tissue compatibility.

To visually evaluate the photothermal thrombolytic effect, we collected lower extremity venous sections from mice subjected to different treatments and performed H&E staining (Fig. 6d). The results showed that the group treated with SQ-BiPh NPs combined with laser irradiation exhibited the most pronounced thrombus dissolution. This process, visualized in real-time *via* NIR-II imaging, vividly demonstrates the potential of SQ-BiPh NPs for thrombus diagnosis and treatment.

Ex vivo fluorescence imaging of major organs revealed that SQ-BiPh NPs were primarily distributed in the liver and spleen, with a gradual decrease in NIR-II signal over time (Fig. S24, SI), consistent with the typical metabolic pattern of nanoparticles. In a mouse tail bleeding assay, the bleeding time of the SQ-BiPh NPs group was similar to that of the PBS control group (Fig. 6e and f), indicating negligible bleeding risk. This characteristic highlights the advantage of photothermal thrombolysis over

conventional drug-based thrombolysis in avoiding hemorrhagic complications.

Furthermore, no significant differences were observed in blood biochemical markers or H&E staining of major organs between the SQ-BiPh NPs-treated group and the control group (Fig. S25 and S26, SI), further confirming the biosafety of this nanosystem and supporting its potential for clinical translation.

Conclusions

In summary, we have successfully developed a novel NIR-II emissive squaraine-based nanoprobe, SQ-BiPh NPs, through rational molecular engineering of the benzo[*cd*]indol-2(1*H*)-one scaffold. The strategic incorporation of a biphenyl unit at the 6-position extends the π-conjugation and enhances molecular planarity, resulting in a bathochromic shift in absorption/emission and a significant increase in molar extinction coefficient. The molecule exhibits unique J-aggregate assembly characteristics upon nanoencapsulation, and this ordered arrangement not only drives the absorption/emission to significantly red-shift into the NIR-II region, but also simultaneously endows the material with excellent photothermal conversion performance. The resulting SQ-BiPh NPs exhibit outstanding NIR-II fluorescence brightness, high photothermal conversion efficiency, and favorable physicochemical properties for biological applications, making them a promising platform for real-time, image-guided precision thrombolysis. Comprehensive *in vitro* and *in vivo* evaluations demonstrate that SQ-BiPh NPs function as an efficient theranostic system capable of integrating real-time NIR-II vascular imaging with highly controlled photothermal thrombolysis. This capability enables dynamic monitoring of thrombus dissolution and vascular recanalization, addressing a critical unmet need in precision thrombosis therapy. The excellent biosafety profile of SQ-BiPh NPs, validated through rigorous cytotoxicity, hemocompatibility, and histopathological assessments, along with its minimal bleeding risk, positions it as a superior alternative to conventional thrombolytic strategies. This work not only presents a robust candidate for next-generation clinical thrombus management but also establishes, through molecular planarization engineering-induced J-aggregate formation, a generalizable molecular design paradigm for advanced NIR-II phototheranostic agents. By enabling real-time, image-guided precision thrombolysis, the SQ-BiPh NPs platform offers a transformative approach for the treatment of thrombotic diseases, with potential applications in pulmonary embolism and atherosclerosis therapy.

Ethical statement

The animal experimental protocol for this study was approved by the Institutional Animal Care and Use Committee (IACUC) of Nanchang University (Approval No. NCULAE-20230610005). All experimental procedures were conducted in strict accordance with national regulations and international guidelines for animal research.

Author contributions

W. H. conceived and designed the experiments for this project. Z. G. performed the synthetic work, while S. L., and Z. F. carried out the characterization of the compounds. Z. G., S. X., and also contributed to the photophysical experiments. Data analysis was conducted by W. H., and Z. G., additionally, W. H. performed the quantum-chemical calculations. W. H., and Z. G., prepared the initial manuscript, with all other authors contributing to revisions. All authors discussed the results and provided feedback on the manuscript.

Conflicts of interest

There are no conflicts to declare.

Data availability

CCDC 2386554 (SQ-H-S), 2386555 (SQ-Ph-S) and 2472690 (SQ-BiPh-S) contain the supplementary crystallographic data for this paper.[48a–c]

The authors declare that all data supporting the findings of this study are available within this article and supplementary information (SI). Supplementary information is available. See DOI: https://doi.org/10.1039/d6sc00914j.

Acknowledgements

The authors thank the National Natural Science Foundation of China (No. 22063005), the Natural Science Foundation of Jiangxi Province (No. 20252BAC250135 and 20212ACBA203012), the Jiangxi Provincical Key Laboratory of Functional Crystalline Materials Chemistry (No. 2024SSY05162) for supporting this work.

Notes and references

1 B. Engelmann and S. Massberg, *Nat. Rev. Immunol.*, 2013, **13**, 34–45.
2 W. E. Winter III, G. L. Maxwell, C. Tian, M. J. Sundborg, G. S. Rose, P. G. Rose, S. C. Rubin, F. Muggia and W. P. McGuire, *J. Clin. Oncol.*, 2008, **26**, 83–89.
3 Q. Wen, Y. Zhang, C. Li, S. Ling, X. Yang, G. Chen, Y. Yang and Q. Wang, *Angew. Chem., Int. Ed.*, 2019, **58**, 11001–11006.
4 Y. Wang, N. Gong, Y. Li, Q. Lu, X. Wang and J. Li, *J. Am. Chem. Soc.*, 2020, **142**, 1735–1739.
5 J. Xu, J. Zhou, Y. Zhong, Y. Zhang, J. Liu, Y. Chen, L. Deng, D. Sheng, Z. Wang, H. Ran and D. Guo, *ACS Appl. Mater. Interfaces*, 2017, **9**, 42525–42535.
6 Y. Li, J. Gao, S. Wang, M. Du, X. Hou, T. Tian, X. Qiao, Z. Tian, P. J. Stang, S. Li, X. Hong and Y. Xiao, *J. Med. Chem.*, 2022, **65**, 2078–2090.
7 Y. Cheng, J. Dai, C. Sun, R. Liu, T. Zhai, X. Lou and F. Xia, *Angew. Chem., Int. Ed.*, 2018, **57**, 3123–3127.
8 H. P. Ebben, V. Jongkind, W. Wisselink, A. W. J. Hoksbergen and K. K. Yeung, *Eur. J. Vasc. Endovasc. Surg.*, 2019, **57**, 667–675.

9 L. Si, J. Tang, K. Yang, M. Wang, Y. Wang, G. Xia and H. Wang, *Chem. Sci.*, 2025, **16**, 7077–7086.
10 P. Cen, J. Huang, C. Jin, J. Wang, Y. Wei, H. Zhang and M. Tian, *Aggregate*, 2023, **4**, e352.
11 A. Ji, H. Lou, C. Qu, W. Lu, Y. Hao, J. Li, Y. Wu, T. Chang, H. Chen and Z. Cheng, *Nat. Commun.*, 2022, **13**, 3815.
12 J. Luo, Z. Xie, J. W. Y. Lam, L. Cheng, B. Z. Tang, H. Chen, C. Qiu, H. S. Kwok, X. Zhan, Y. Liu and D. Zhu, *Chem. Commun.*, 2001, 1740–1741.
13 K. Welsher, Z. Liu, S. P. Sherlock, J. T. Robinson, Z. Chen, D. Daranciang and H. Dai, *Nat. Nanotechnol.*, 2009, **4**, 773–780.
14 S. He, S. Chen, D. Li, Y. Wu, X. Zhang, J. Liu, J. Song, L. Liu, J. Qu and Z. Cheng, *Nano Lett.*, 2019, **19**, 2985–2992.
15 Y. Liu, Y. Yuzhen, T. Tian, W. Wang, J. Nong, X. Qiao, F. Xu, J. Gao and X. Hong, *Chin. Chem. Lett.*, 2021, **32**, 3061–3065.
16 W. Shao, Q. Wei, S. Wang, F. Li, J. Wu, J. Ren, F. Cao, H. Liao, J. Gao, M. Zhou and D. Ling, *Mater. Horiz.*, 2020, **7**, 1379–1386.
17 P. Chen, L. He, K. Chen, Q. Pan, J. Rong, Q. Mei, P. Sun, C. Zhang and D. Li, *Biomaterials*, 2025, **323**, 123435.
18 S. Xu, Y. Duan and B. Liu, *Adv. Mater.*, 2020, **32**, 1903530.
19 J. Yan, X. Rodríguez-Martínez, D. Pearce, H. Douglas, D. Bili, M. Azzouzi, F. Eisner, A. Virbule, E. Rezasoltani, V. Belova, B. Dörling, S. Few, A. A. Szumska, X. Hou, G. Zhang, H.-L. Yip, M. Campoy-Quiles and J. Nelson, *Energy Environ. Sci.*, 2022, **15**, 2958–2973.
20 Y. Zhao, R.-R. Zhang, N. Wang, X.-L. Tian, L.-N. Zhang, W.-L. Xia, Z.-Y. Wang, X.-Q. Yu and K. Li, *Mater. Horiz.*, 2025, **12**, 10698–10708.
21 S. Chen, Y. Pan, K. Chen, P. Chen, Q. Shen, P. Sun, W. Hu and Q. Fan, *Angew. Chem., Int. Ed.*, 2023, **62**, e202215372.
22 M. Yang, X. Ou, J. Zhang, J. Sun, R. T. K. Kwok, J. W. Y. Lam, J. Fan and B. Z. Tang, *Adv. Funct. Mater.*, 2025, **35**, 2411838.
23 J. Tang, L. Si, Y. Wang, G. Xia and H. Wang, *Adv. Healthcare Mater.*, 2025, **14**, 2404322.
24 J. Luo, K. Huang, X. Yi, P. Lu, H. Xie, W. Li, Q. Zeng, F. He, D. Wang and L. Wang, *Adv. Sci.*, 2026, **13**, e12764.
25 M. J. Abraham, T. Murtola, R. Schulz, S. Páll, J. C. Smith, B. Hess and E. Lindahl, *SoftwareX*, 2015, **2**, 19–25.
26 S. Ma, Y. Liu, J. Zhang, B. Xu and W. Tian, *J. Phys. Chem. Lett.*, 2020, **11**, 10504–10510.
27 J. Song, H. Wang, X. Meng, W. Li and J. Qi, *Nat. Commun.*, 2024, **15**, 10395.
28 C. Wang, W. Zhong, X. Sun, J. Guo, Y. Chen, Y. Zhao, J. Han and Y. Zhao, *Angew. Chem., Int. Ed.*, 2025, **64**, e202416828.
29 Z. Xu, X. Li, Z. Yang, Z. Zhang, Y. Zhang, M. Fan, Y. Zeng, M. Kang, Y. Shen, D. Wang, G. Xu and B. Z. Tang, *Adv. Mater.*, 2025, **37**, 2413164.
30 D. Chang, J. Yang, Y. Li, S. Min, Y. Ma, T. Xu, Z. Zhang, X. Zhu, X. Xu, C. Lu, B. Zhao, M. Chen, Z. Xiao, J. Xie and S. Ju, *ACS Nano*, 2025, **19**, 36323–36341.
31 H. Dai, J. Shao, D. Lei, K. Xu, T. Zhang, A. Mei, P. Chen, Y. Guo and X. Dong, *ACS Nano*, 2025, **19**, 35842–35852.
32 H. Gao, Y. Liu, L. Liu, R. Li, D. Tu, Y. Lin and X. Chen, *Aggregate*, 2025, **6**, e70178.
33 Y. Tang, D. Xiang and Q. Li, *Adv. Mater.*, 2025, **37**, 2501184.
34 Q. Wang, J. Liu, L. Yang, Z. Tao, J. Feng, S. Li, X. Wang, L. Gao, W. Tang and Q. Fan, *Adv. Funct. Mater.*, 2025, **35**, 2423165.
35 H. Wen, Z. Deng, R. Dong, Z. Zhang, X. Chen, G. A. Alfani, W.-J. Wang, Z. Qiu, P. Alam, Z. Zhao and B. Z. Tang, *Adv. Funct. Mater.*, 2025, **35**, 2508015.
36 Q. Xu, Y. Wang, Y. Guan, C. Ma, G. Yi, X. Du, H. Bin, W. Shen, C.-Y. Wang, Y. Wu, H. Ma, F. Tong, W.-H. Zhu and W. Zhao, *Angew. Chem., Int. Ed.*, 2026, **65**, e202522144.
37 Y. Xu, D. An, T. Zhang, X. Wu, S. Wang, J. Shao, L.-L. Qu, Y. Guo and X. Dong, *Adv. Mater.*, 2025, **37**, 2418894.
38 L. Yang, J. Huang, Y. Liao, D. Hu, Y. He, N. Feng, R. T. K. Kwok, J. W. Y. Lam, J. Zhang, B. He and B. Z. Tang, *Adv. Healthcare Mater.*, 2025, **14**, 2500513.
39 Q. Yu, Y. Zhou, Q. Zhang, J. Li, S. Yan, J. Xu, C. Li, X. Zhou and Y. Sun, *Biomaterials*, 2025, **322**, 123381.
40 L. Zhao, H. Zhu, Q.-Q. Ye, Z.-G. Wang, D.-W. Pang, D. Ding and S.-L. Liu, *J. Med. Chem.*, 2025, **68**, 23610–23619.
41 D. Zhou, J. Tong, L. Zhang, Y. Yao, Y. Gao, Y.-C. Wang, G. Xu, G. Shan and L. Ren, *Biomaterials*, 2026, **326**, 123693.
42 S. Ning, P. Shangguan, X. Zhu, X. Ou, K. Wang, M. Suo, H. Shen, X. Lu, X. Wei, T. Zhang, X. Chen and B. Z. Tang, *J. Am. Chem. Soc.*, 2025, **147**, 7433–7444.
43 P. R. Spackman, M. J. Turner, J. J. McKinnon, S. K. Wolff, D. J. Grimwood, D. Jayatilaka and M. A. Spackman, *J. Appl. Crystallogr.*, 2021, **54**, 1006–1011.
44 Y. Chen, S.-Y. Yang, X. Ou, H. Wang, F.-C. Kong, P. C. Y. Chow, Y. Wang, Y. Jiang, W. Zhao, J. Sun, R. T. K. Kwok, D.-W. Zheng, W. Yu, F. Wang, J. W. Y. Lam and B. Z. Tang, *J. Am. Chem. Soc.*, 2024, **146**, 35462–35477.
45 Z. He, Y. Gao, Z. Huang, M. Zhan, S. Tian, F. Fang, D. Zhao, Z. a. Li, F. Meng, B. Z. Tang and L. Luo, *ACS Nano*, 2025, **19**, 10220–10231.
46 W. Li, S. Ai, H. Zhu and W. Lin, *Nat. Commun.*, 2025, **16**, 2471.
47 H. Shen, X. Zhu, J. Zhang, C. Xu, J. W. Y. Lam and B. Z. Tang, *Small*, 2025, **21**, 2411866.
48 (*a*) J. Tang, L. Si, Y. Wang, G. Xia and H. Wang, CCDC 2386554: Experimental Crystal Structure Determination, *Adv. Healthcare Mater.*, 2024, 2404322, DOI: 10.1002/adhm.202404322; (*b*) J. Tang, L. Si, Y. Wang, G. Xia and H. Wang, CCDC 2386555: Experimental Crystal Structure Determination, *Adv. Healthcare Mater.*, 2024, 2404322, DOI: 10.1002/adhm.202404322; (*c*) CCDC 2472690: Experimental Crystal Structure Determination, 2026, DOI: 10.5517/ccdc.csd.cc2p016z.